



City Research Online

City St George's, University of London

Citation: Fostiropoulos, S., Strotos, G., Nikolopoulos, N. & Gavaises, M. (2020). Numerical investigation of heavy fuel oil droplet breakup enhancement with water emulsions. *Fuel*, 278, 118381. doi: 10.1016/j.fuel.2020.118381

This is the accepted version of the paper.

This version of the publication may differ from the final published version. To cite this item please consult the publisher's version.

Permanent repository link: <https://openaccess.city.ac.uk/id/eprint/25111/>

Link to published version: <https://doi.org/10.1016/j.fuel.2020.118381>

Copyright and Reuse: Copyright and Moral Rights remain with the author(s) and/or copyright holders. Copies of full items can be used for personal research or study, educational, or not-for-profit purposes without prior permission or charge, unless otherwise indicated, provided that the authors, title and full bibliographic details are credited, a hyperlink and/or URL is given for the original metadata page and the content is not changed in any way. For full details of reuse please refer to [City Research Online policy](#).

1 Numerical investigation of Heavy Fuel Oil droplet breakup enhancement with 2 water emulsions

3

4 Stavros Fostiropoulos^{*1,2}, George Strotos³, Nikolaos Nikolopoulos¹ and Manolis Gavaises²

5 ¹Centre for Research and Technology Hellas/Chemical Process and Energy Resources Institute (CERTH/CPERI),
6 Egialeias 52, Marousi, Greece

7 ²City University of London, School of Engineering and Mathematical Sciences, Northampton Square, EC1biliv 0HB
8 London, UK

9 ³University of Thessaly, 41110 Larissa, Greece

10 *Corresponding author: fostiropoulos@certh.gr

11

12 Abstract

13 The heating and explosive boiling leading to fragmentation of immiscible heavy fuel oil-water droplets, termed as
14 W/HFO emulsions, is predicted numerically by solving the incompressible Navier-Stokes and energy equations
15 alongside with a set of three VoF transport equations separating the interface of co-existing HFO, water liquid and
16 water vapour fluid phases. Model predictions suggest that explosive boiling of the water inside the surrounding
17 HFO, ought to their different boiling points, accelerates droplet breakup; this process is termed as either puffing or
18 micro-explosion. In contrast to past studies which predefine the presence of vapor bubbles inside the water droplet,
19 this is predicted here with a phenomenological model based on local temperature and superheat degree. Following
20 their formation, the growth rate of the bubbles is computed with OCASIMAT phase-change algorithm. Moreover,
21 the fuel droplet is simultaneously subjected to convective air flow which further contributes to its deformation. As
22 a result, the performed simulations quantify the relative time scales of the aerodynamic-induced and the emulsion-
23 induced breakup mechanisms. The conditions examined refer to a highly viscous emulsified heavy fuel oil droplet
24 in a gas phase having fixed temperature and pressure equal to 1000 K and 30 bar, respectively. Initially, a benchmark
25 case demonstrates the detailed mechanisms taking place, concluding that droplet fragmentation occurs only at a
26 part of the fuel-air interface, resembling characteristics similar to puffing. Next, a parametric study with Weber
27 number ($Oh = 0.9, We < 200$) shows that puffing process can speed up to 10 times the breakup of the droplet
28 relative to aerodynamic breakup.

29

30 Keywords: CFD, fuel oil-water emulsion, breakup, VoF, vapor nucleation, boiling

31

32

33

34

35

36

37

38

39

40

41

42

43

44

45

46 **Nomenclature**

Roman symbols

<i>a</i>	Thermal diffusivity [m^2s^{-1}]
<i>A</i>	Interfacial surface area [m^2]
<i>b</i>	Scriven bubble growth factor
<i>c_p</i>	isobaric heat capacity [$\text{J kg}^{-1} \text{K}^{-1}$]
<i>d</i>	Distance [m]

Subscripts

∞	far-field quantity
0	initial value
b	bubble
br	breakup
c	critical

D	Diameter [m]	CFD	values provided by CFD
E	Energy [J]	dr	water sub-droplet
f	Physical variable	g	gas
h_{lv}	heat of vaporization [J kg^{-1}]	i	interface
k	thermal conductivity [$\text{W m}^{-1} \text{K}^{-1}$]	l	liquid
m	mass [kg]	m	mass-averaged
Oh	Ohnesorge number	oil	Oil phase/droplet
p	pressure [Pa]	q	phase number
Pe	Peclet number	s	surface
R	radius [m]	sat	saturated
Re	Reynolds number	sh	Shear
St	Stefan number	v	Vapor
t	time	w	water
T	temperature [K]		
u	Velocity [ms^{-1}]		
V	Volume [m^3]	Dotted symbols	
We	Weber number	$\dot{\phi}$	first time derivative
		$\ddot{\phi}$	second time derivative

Greek symbols

α	Volume fraction
ΔT_s	Superheat degree [K]
μ	Dynamic viscosity [Pa s]
ρ	density [kg m^{-3}]
σ	Surface tension [N m^{-1}]

47

48 **1. Introduction**

49 Across the world, and despite the increasing fraction of electric vehicles (EVs) (they are expected to reach 60% in
50 passenger car and light duty vehicles and up to 15% for heavy duty over the next two decades [1, 2] the forecasted
51 increase of liquid fossil fuel usage will be 25% globally and more than 50% for heavy-duty vehicles over the same
52 time period; this is due to the constantly increasing global energy needs, urbanisation and population growth [3].
53 Diesel engines are massively used as a source of power, especially for transportation, due to their relatively high
54 power output and fuel economy [4]; however, electrification in this transport/power sector is expected to be a
55 long-term process. Combustion products from Diesel engines, especially, NO_x and particulate matter (PM), are
56 known to be harmful to both the environment and directly to human health when inhaled. According to [5],
57 anthropogenic emissions contribute more than 90% to the climate change while Diesel engines are responsible for
58 $\sim 2/3$ of the total liquid fossil fuel utilization globally. Besides the environmental impact, lung cancer, asthma and
59 cardiovascular diseases are linked to such emissions. The aforementioned concerns have triggered many research
60 efforts investigating mechanisms for reducing the in-cylinder formed pollutants in heavy duty and marine Diesel

61 engines [6, 7]; among them, water emulsions into heavy fuels is known to offer significant simultaneous reduction
62 in NO_x and PM emissions [8].

63 Water can be introduced to the engine by three common methods: (i) emulsified fuel-water in Diesel emulsion
64 (WiDE); (ii) in-cylinder water injection [9]; and (iii) water injection into the intake air (fumigation) [10]. In both
65 fumigation and direct water injection, water is in direct contact with the fuel injection system and the piston
66 cylinder which may cause oil contamination and corrosion issues. Thus, the most promising approach to utilise
67 water for reduction of emissions is considered to be the WiDE method [11, 12]. The fact that no engine modification
68 is required, points out water-emulsified fuels as a cost-effective solution. On the other hand, both fumigation and
69 direct water injection demand engine modification, which has high additional cost [13].

70 Emulsion is generated by means of mechanical agitation in the presence of surface active agents, called surfactants
71 or emulsifiers. The latter are needed in order to avoid the coalescence of the water sub-droplets. When an
72 emulsified droplet is injected inside a combustion chamber, heat is transferred from the hot ambient air to the
73 emulsified droplet. The host (parent) droplet has higher boiling point than the corresponding one of the water sub-
74 droplet; the water sub-droplet becomes superheated and eventually boils (Figure 1). The water droplet is contained
75 in a uniform substance (oil droplet) free of nucleation sites and for that reason it is capable of exceeding its boiling
76 point and experiences a metastable regime. At some point though, as the droplet heats up and the local
77 temperature exceeds the boiling point of water, homogeneous nucleation occurs (in contrast to heterogeneous
78 boiling which occurs when a fluid is in contact with solid surfaces) and water starts to boil [14]. Vapor generation
79 leads to expansion and deformation of the surrounding oil droplet and eventually leads to its fragmentation. Micro-
80 explosion is defined as the process during which complete breakup of the oil droplet occurs, while if just a portion
81 of the oil droplet is ruptured, the process is termed as puffing. The aforementioned breakup regimes have been
82 widely discussed in the literature, see selectively [12, 15, 16].

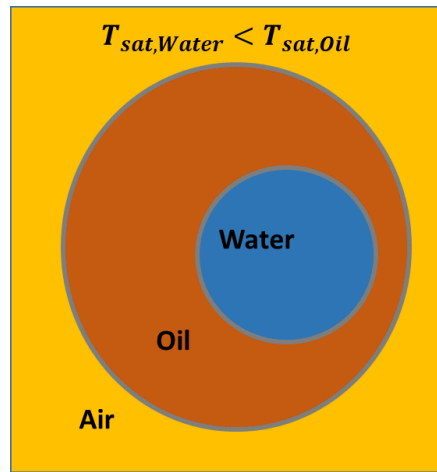


Figure 1. Emulsion droplet indicative configuration

83

84

85

86 Despite the potential benefit of using emulsified fuels, the detailed physical mechanisms that occur during micro-
 87 explosion and puffing are not clear. In the experimental work of [17], homogeneous explosive boiling of a vapor
 88 bubble inside a superheated water droplet has been studied and the size of the vapor bubble during its growth was
 89 measured. In a similar experiment by [18], it was observed that during explosive boiling, liquid particles were torn
 90 from the liquid-gas interface, alongside with bubble oscillations. So far, the majority of experiments on emulsion
 91 droplets has focused on the combustion characteristics after the puffing/micro-explosion induced secondary
 92 atomisation [19-21]; thus, the overall dynamics of a single droplet cannot be revealed. In single droplet
 93 experiments, a relative large droplet (O (1 mm)) compared to those realized in engines has been investigated. In
 94 the work of [22] it was found that the water volume fraction and the quantity of surfactant may influence the
 95 tendency towards micro-explosion. The latter can also be affected by the size distribution of the dispersed water
 96 sub-droplets [23]. Recently, single droplet experiments having sizes similar to those realised in diesel engines (O
 97 (10 μm)), were performed by [24, 25]. In the experiment of [25], the effect of water content on the characteristics
 98 of micro-explosion was investigated, using a high speed video camera. However, the physical processes taking place
 99 inside the emulsion and during the growth rate of the boiling water have not been revealed.

100 The factors that influence the growth rates of boiling bubbles in pool liquids have been extensively studied over the
 101 last 50 years. In general, density fluctuations and disturbances are always present in liquids and are responsible for
 102 the formation of bubble nuclei. Nano or sub- μm vapor bubble nuclei collapse and disappear due to Laplace pressure

103 in an accelerated manner; however, some of them may pass a critical radius ($R_0 = 2\sigma/\Delta P_0$) and continue to grow.
104 The aforementioned expression must be couched in terms of the probability that a bubble with R_0 will occur at the
105 time where a critical pressure difference ΔP_0 is applied. According to [26], liquids are able to withstand pressure
106 differences of $3 \cdot 10^4$ to $3 \cdot 10^5$ bar, which correspond to a critical bubble radius comparable to the intermolecular
107 distance (10^{-10} m). Since the vapor bubble has passed its critical radius, it continues growing in three different
108 phases. The first growth phase is surface tension dominated where the pressure difference is balanced by the
109 surface tension, while the bubble has the same temperature as the surrounding liquid. That regime diminishes
110 quickly as the bubble size increases. Next, the bubble growth is limited by the inertia of the surrounding liquid and
111 the bubble radius is a linear function of time. The bubble continues expanding, while its surface temperature
112 decreases due to evaporation. The internal bubble pressure decreases until the driving force due to pressure
113 difference is negligible. The final phase of growth is “diffusion” controlled, where bubble surface temperature will
114 reach the bulk saturation temperature, and the growth is limited by heat diffusion. At this regime, the growth rate
115 of bubble decreases substantially; the bubble radius R increases with \sqrt{t} instead of t . Theoretical models have been
116 developed in the past that accurately predict vapor bubble growth in either inertial [27] or diffusive [28-31] regime.
117 In the work of [32], a solution is obtained that combines the works of [27] and [29] and manages to predict
118 successfully the bubble growth rate in both inertial and diffusion dominated regimes. According to this study, the
119 critical radius (eq. 1) that defines the transition from the inertial to the diffusion-controlled regime is determined
120 by the fluid properties and the liquid superheat:

$$R_c = 2\sigma T_{sat} / h_{lv} \rho_v \Delta T_s \quad (1)$$

121 The latter size is significant for the development of the current CFD model, since the initial bubble size in the
122 simulations is assumed to be diffusion-controlled in order to be capable to resolve it.

123 The development of micro-explosion models could shed light on the relevant processes. One of the first emulsion
124 mathematical models is that of [33], which predicts the vapor bubble growth ought to homogeneous nucleation
125 within a liquid water droplet. However, puffing/micro-explosion phenomenon was not taken into account. A similar
126 approach was followed by [34], who employed Rayleigh’s model to predict vapor bubble growth in the centre of a
127 liquid water droplet; however, the assumptions made in that model (e.g. the droplet is stationary) may not be

128 suitable for engine fuel spray conditions. Simplified mathematical models which can be useful for engineering
129 applications have also been suggested [35, 36], but they cannot provide details of the physical processes during
130 deformation and breakup of emulsion droplets. Finally, advanced CFD models proposed recently by [15, 16] gave
131 insight on the underlying physics of micro-explosion and puffing. In the work of [15], simulations of a static emulsion
132 droplet have been performed where the latter is considered to be preheated in the boiling temperature of its
133 embedded water sub-droplet. Besides the predefined temperature, the location and size of the vapor bubble were
134 also predefined. Convective heating of emulsion droplets has been studied in [16]; the model predictions indicated
135 that the boiling of the embedded water sub-droplet highly depends on the liquid Peclet number and the internal
136 circulation inside the parent droplet.

137 Droplet secondary breakup due to aerodynamic forces is typically characterized by the Weber (We) and Ohnesorge
138 (Oh) numbers (i.e it is controlled by inertia, surface tension and viscous forces), as also by the Reynolds number
139 and the liquid to gas density (ϵ) and viscosity (N) ratios [37], which play a secondary role. Breakup results in droplet
140 fragmentation into several smaller droplets and requires a finite time of the order of the shear breakup timescale
141 ($t_{sh} = D\sqrt{\epsilon}/u$) [38] to be completed. For the case of emulsified droplets, a crucial question arises: is there enough
142 time for the droplet to heat-up, nucleation sites to appear and explosive boiling to occur, when the former is
143 subjected to aerodynamic forcing? To the best of our knowledge, the aforementioned physical processes have only
144 been addressed independently, with the aid of simplified mathematical models [33, 36, 39, 40].

145 The aim of the present study is to clarify this question; from a physical standpoint, the current work addresses the
146 combined effect of thermal (due to micro-explosion) and aerodynamic secondary droplet breakup processes, with
147 the aid of a CFD model capable of simulating the overall phenomenon, starting from convective heating of the
148 emulsion droplet up to puffing/micro-explosion. The model considers vapor generation and edge regression of
149 W/HFO interface and captures the puffing/micro-explosion-induced droplet fragmentation. Moreover, and unlike
150 previous studies, the vapor nucleation sites are not predefined, but they are predicted as part of the solution, based
151 on the local liquid temperature. The examined properties are similar to that of a highly viscous HFO, which is
152 typically used in large marine Diesel engines. HFO is treated here as single component, thus species distribution
153 inside the parent droplet is not considered. As aforementioned, homogeneous nucleation occurs when a tiny vapor

154 nucleus is generated inside a uniform liquid. Emulsion experiments have shown that the probability of vapor
155 nucleation is related to the temperature of the liquid, while the vapor nuclei are generated close to the water
156 interface [41, 42]. Since it is difficult to resolve the vapor nucleation phenomenon, a mechanistic algorithm that
157 accounts for the initial formation of a small vapor bubble and takes into account the aforementioned experimental
158 findings, has been developed and implemented into the CFD code.

159 In the following section the mathematical description of the emulsion droplet breakup model is provided, alongside
160 with the vapor bubble formation algorithm and the OCASIMAT phase-change model for vapor bubble growth [43].
161 Examined cases and results are following, while the most important conclusions are summarized in the end.

162

163 **2. Numerical model and methodology**

164 *2.1 Volume of Fluid method*

165 The numerical technique that is used in this study for tracking the interface between multiple fluids/phases is the
166 Volume of Fluid method [44]. The VoF method solves a single set of momentum equations and identifies each fluid
167 by a volume fraction denoted by α . Specifically, in the emulsion model three phases initially exist (Air, Oil, Water)
168 and at some point during the simulation an additional phase is solved due to sudden appearance of vapor. The
169 volume fraction α is defined as the percentage of volume covered by each phase in the computational cell with
170 respect to the total volume of the cell. In each cell the sum of the volume fractions of all phases must be equal to
171 unity. Mathematically, when volume fraction of phase q inside a cell is unity, the cell is completely covered by the
172 material of phase q , while when the volume fraction is equal to zero, the cell is empty of phase q . Finally, when the
173 volume fraction of q^{th} fluid is between 0 and 1, the cell contains the interface between the q^{th} fluid and one or
174 more other fluids. Upon the volume fraction value of phase q , variables and properties represent volume-averaged
175 values of phase q . For instance, the physical variable f within a computational cell will be computed as follows:

$$f = \sum_{q=1}^N \alpha_q f_q, \text{ where } N = \text{number of phases} \quad (2)$$

176 The advection equation for the volume fraction is defined as:

$$\frac{\partial a_q}{\partial t} + \nabla \cdot (\vec{u}_q a_q) = \frac{\dot{m}_{pq}}{\rho} \nabla a_q \quad (3)$$

177 where the term in the RHS stands for any additional volumetric mass source term.

178 A single momentum equation is solved throughout the entire numerical domain, and the computed velocity field is
 179 shared among all the phases. The momentum equation is dependent on the properties of density ρ and dynamic
 180 viscosity μ , which are computed according to Eq. 2, and it is written in the form:

$$\frac{\partial(\rho \vec{u})}{\partial t} + \nabla \cdot (\rho \vec{u} \otimes \vec{u} - \vec{T}) = \rho \vec{g} - \vec{f}_\sigma \quad (4)$$

181 where \vec{T} is the stress tensor and \vec{v} is the velocity. Surface tension term denoted as \vec{f}_σ is taken from [45] and for the
 182 case that only two phases are present inside a computational cell, the relation reads:

$$\vec{f}_\sigma = \sigma_{pq} \frac{\rho \kappa_p \nabla a_p}{\frac{1}{2}(\rho_p + \rho_q)} \quad (5)$$

183 where κ is the curvature of the free surface, approximated as the divergence of unit surface normal "n", and reads:

$$\kappa_p = \nabla \cdot \hat{n} \quad (6)$$

184

$$\hat{n} = \frac{\nabla a_p}{|\nabla a_q|} \quad (7)$$

185 The energy equation, which is also shared among the contributing phases, is presented in Eq.8, where energy E is
 186 a mass-averaged variable between each additional phase:

$$\frac{\partial(\rho E)}{\partial t} + \nabla \cdot (\vec{u}(\rho E + p)) = \nabla \cdot (k_{eff} \nabla T) + S_h \quad (8)$$

187

$$E = \frac{\sum_{q=1}^n \alpha_q \rho_q E_q}{\sum_{q=1}^n \alpha_q \rho_q} \quad (9)$$

188 In the equations above, density ρ and effective thermal conductivity, denoted by k_{eff} , are shared among the
189 phases. Finally, S_h contains contributions from any volumetric heat sources existed in the model. The solution
190 methods selected alongside with the numerical details are provided in the following sections.

191

192 2.2 Vapor bubble formation and growth

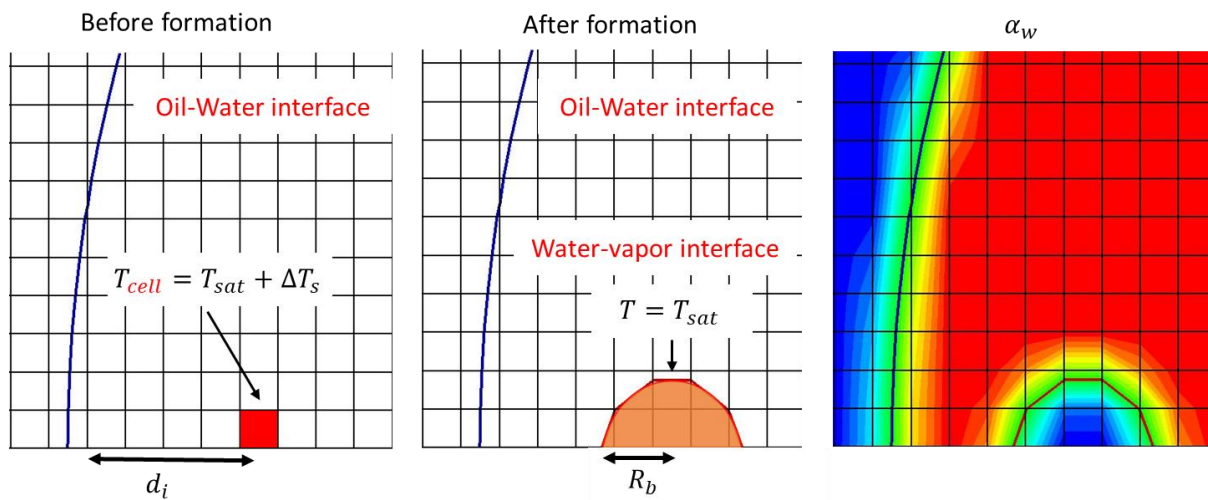
193 As nucleation theories aiming to resolve formation of vapor nuclei inside the bulk of the water are out of scope of
194 the present work, a conceptual approach for vapor bubble formation is developed and implemented in the CFD
195 model. The criteria under which a vapor bubble is generated are the following. First, the formation site, which is a
196 computational cell (Figure 2; left panel), should be located at a specific distance (d_i) from the oil-water interface
197 [18]. This distance has a finite length preventing contact of the bubble with the oil-water interface (Figure 2; Right
198 panel). In case that vapor, water and oil phases coincide in a computational cell, numerical issues arise. A relevant
199 parametric study with bubble's surface depth is presented in Appendix A, proving that the obtained results are not
200 sensitive to this numerical selection. Next, the superheat degree (ΔT_s) of vapor generation is also an input
201 parameter of the model. The algorithm checks if the selected superheat degree has been reached in the
202 aforementioned computational cell. Different superheat values from 5 to 25 K have been examined but the results
203 seem not to be sensitive (Appendix A). Once the aforementioned criteria are fulfilled in a computational cell, a
204 bubble is formed at the center of the computational cell. As discussed in the literature, the vapor bubble should
205 reach a critical size ($R_0 = 2\sigma/\Delta P_0$) in order to start growing and not collapsing immediately due to surface tension.
206 The first growth phase is inertia-controlled, which ends quickly (typically $\sim 0.1 \mu s$) and diffusion-controlled growth
207 follows. The transition to the diffusive regime is characterized by a critical bubble radius [32], which depends on
208 fluid properties and liquid superheat. In the examined cases of the current study that radius was computed to be
209 of the order of $0.11 \mu m$ (eq. 1). As it's computationally expensive to resolve such a length scale, the vapor bubble
210 is initiated with a finite radius size ($R_{b,0} = 0.25 \mu m$). It should be noted that the influence of the initial bubble
211 radius on the obtained results has been checked by performing numerical experiments, pointing out that the
212 breakup process is identical and only the early development of the bubble differs; similar behavior has been
213 observed also in the work of [15]. Since the initial bubble starts growing due to heat diffusion, as it is larger than

214 R_c , a bulk saturation temperature value is imposed at its interface (506 K), while its internal pressure is defined by
 215 the surface tension term ($2\sigma/R_{b,0}$). The latter is calculated to be 2 bar. A schematic configuration of vapor bubble
 216 formation is illustrated in Figure 2.

217 Summarizing, the criteria for bubble creation in a computational cell are the following: i) $T_{cell} \geq T_{sat} + \Delta T_s$, ii) d_i
 218 to be the smallest possible, without vapor water and oil coexisting in a computational cell (in the current resolution
 219 $R_{b,0} = 0.25 \mu\text{m}$ as already mentioned).

220

221



222

Figure 2. Configuration of vapor bubble formation

223

224 Right after its formation, the vapor bubble starts growing due to interfacial heat and mass transfer. A method
 225 termed as OCASIMAT [43] is implemented in the CFD model and calculates the growth rate of the vapor bubble. So
 226 far, different computational methods have been proposed for the computation of heat and mass transfer rate
 227 during boiling. In many studies [46-48], that rate is computed by assuming a temperature difference between the
 228 liquid-vapor interface and a saturation temperature; the calculation depends on an empirically derived
 229 accommodation coefficient though. A different approach is to compute the temperature gradients at the center or
 230 faces of the interface cells [49, 50]. The precise location of the interface is ignored, making these methods
 231 computationally inexpensive but not very accurate.

232 The employed method in the current study computes the temperature gradient at the liquid-vapor interface with
233 the temperature of only one computational cell in the liquid side, implying that the temperature of the vapor phase
234 is uniform and equal to the saturation temperature T_{sat} . The interface temperature is also fixed at the saturation
235 point T_{sat} , since the growth is controlled by heat diffusion, while the mass transfer rate (kg/s) is related to the
236 local temperature gradient. Another significant feature of the algorithm is that it introduces a source term in the
237 energy equation, in order to impose an accurate temperature value at the interface cells. This approach assumes
238 that the temperature profile across the interface region is linear, which can be considered as a reasonable
239 assumption as long as the grid is dense. More details about the OCASIMAT algorithm are provided in [43].

240

241 **3. Results and discussion**

242 To the best of our knowledge, suitable data from single emulsion droplet experiments in engine thermodynamic
243 conditions are not available for a direct comparison with the results of the current CFD model. To compare against
244 the experimental results of [51], the simulation of several water sub-droplets is required. This is prohibited since it
245 requires a 3D computational domain with several micro-droplets randomly distributed inside the host droplet that
246 would dramatically increase the computation cost. However, since homogeneous boiling occurs in puffing/micro-
247 explosions, simulation of a simplified configuration has been performed in order to examine if the developed
248 numerical model is capable of reproducing such a phenomenon. The results are compared against an analytical
249 solution.

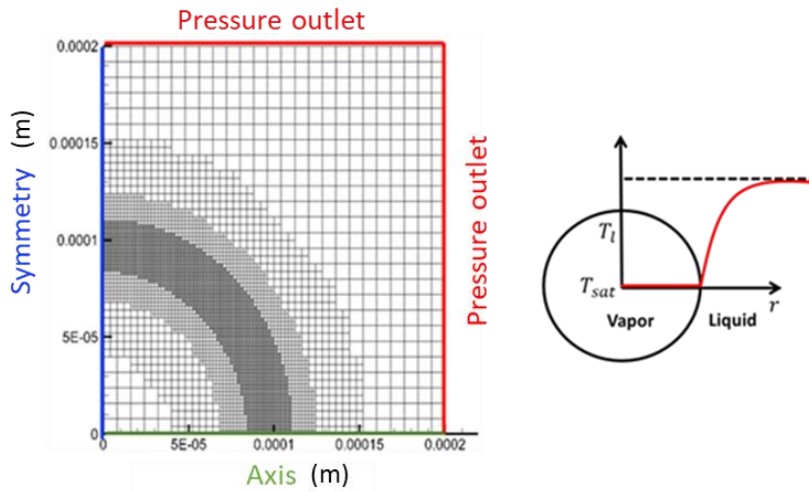
250

251 *3.1 Spherical bubble growth inside an infinite water pool (Homogeneous boiling)*

252 *3.1.1 Computational setup and model validation*

253 Vapor bubble growth inside a superheated liquid pool is investigated using the aforementioned CFD model, while
254 the OCASIMAT algorithm has been implemented for the estimation of mass transfer rate. The latter directly
255 depends on the nondimensional Stefan number ($St = c_{pl}\Delta T_s/h_{lv}$). The flow equations are solved in an

256 axisymmetric domain, where in the left vertical axis, symmetry boundary condition is imposed. All the rest
257 boundaries are open, where velocity 1st gradient is set to zero (Figure 3).



258

259 Figure 3. Computational mesh refined locally alongside with boundary conditions (Left panel). Schematic illustration of
260 thermal boundary layer (Right panel).

261

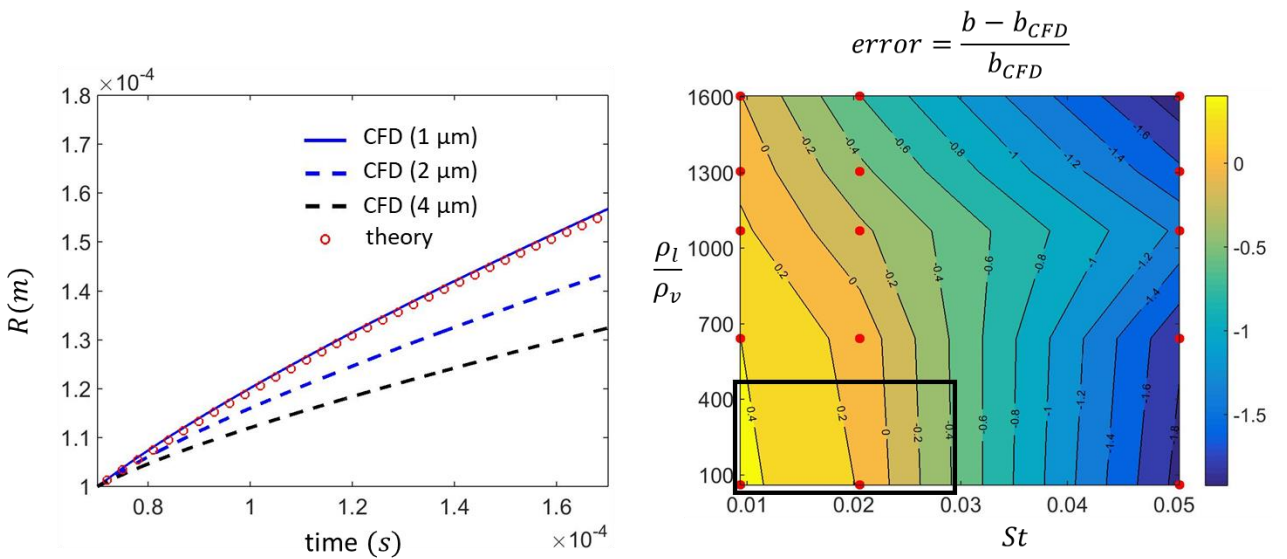
262 The domain extends up to a distance of $2R_0$ in both vertical and horizontal directions; the same configuration has
263 been employed in past studies [43, 47, 49, 52]. In order to save computational cost, an adaptive local refinement
264 method has been employed [53]. From the Mikic relationship [32], it was computed that the transition to the
265 diffusion controlled growth, in the current case, occurs when the bubble radius is equal to $6 \mu\text{m}$. Here, the
266 simulation starts from an initial bubble radius R_0 equal to $100 \mu\text{m}$, where heat diffusion is already dominant and
267 an initial thermal boundary layer (TBL) has been developed in the liquid phase. Moreover, a mesh independence
268 study has been performed in order to retrieve the adequate mesh resolution needed for the TBL to be resolved.
269 The results are compared against an analytical solution, which is described in the following paragraph. For the CFD
270 model to be in agreement with analytical solution, it was found out that the base grid resolution should be 10 cpR
271 with 4 levels of refinement, corresponding to 160 cpR at the beginning of the simulation.

272 The analytical solution for the case of bubble growth inside an infinite liquid is derived by [30]. The solution assumes
273 that the bubble radius is given by the following relationship:

$$R_b = 2b\sqrt{a_w t}$$

$$b = \sqrt{\frac{3}{\pi}} \left\{ \frac{\Delta T_s}{\left(\frac{\rho_g}{\rho_w} \right) \left[\frac{h_{lv}}{c_{p,w}} + \left(\frac{c_{p,w} - c_{p,g}}{c_{p,w}} \right) \Delta T_s \right]} \right\} \quad (10)$$

274 Here, b is a dimensionless bubble growth constant where its value depends on the superheat degree (ΔT_s) and the
 275 thermophysical properties of the material examined. The vapor bubble, with fluid properties corresponding to that
 276 of water at atmospheric conditions, is growing inside a temperature field with superheat degree of 5 K ($St =$
 277 $c_{p,w}\Delta T_s/h_{lv} = 0.01$). Results in the left panel of Figure 4 clearly indicate that the accuracy of the simulation
 278 improves with smaller mesh size. Specifically, for mesh size equal to 1 μm (blue solid line), where the initial thickness
 279 of the thermal boundary layer (TBL) is computed equal to 12 μm , it is observed that the model results are in perfect
 280 agreement with that of the theoretical solution. Next, a number of parametric cases was performed, in order to
 281 examine the model performance for different values of St and density ratios. In order to estimate the deviation of
 282 the CFD model from theory, a bubble growth constant (b_{CFD}) was derived for each parametric case and compared
 283 against the corresponding constant b of the analytical solution. The nondimensional error is expressed as
 284 $b - b_{CFD}/b_{CFD}$ and it seems significant for high Stefan numbers. The error decreases up to a point where mesh
 285 resolution becomes higher. In general, the emulsion droplets are examined for conditions where density ratio is
 286 low, due to high pressure (black rectangular shape); in this range of density ratio and for St up to 0.03, the
 287 computed error is not significant.



288

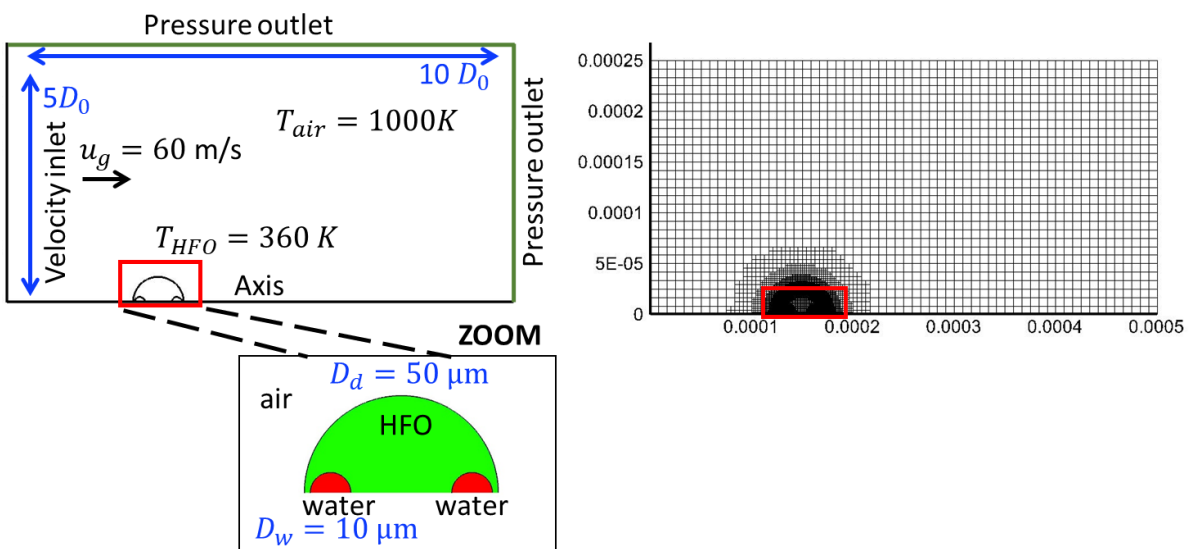
289 Figure 4. Prediction of the bubble growth rate for different grid resolutions (Left panel). Map indicating the error between
290 the predictions of CFD and analytical solution (Right panel)

291

292 3.2 Emulsion breakup subjected to aerodynamic forces

293 3.2.1 Computational setup and examined cases

294 The initial conditions in the numerical domain reflect typical conditions of a HFO droplet inside the combustion
295 chamber of marine Diesel engines [54]. Equations are solved in an axisymmetric domain where the left vertical axis
296 is a velocity inlet boundary that imposes the velocity of the stream flow, while the rest boundaries are open (i.e.
297 velocity gradient is set to zero). The domain extends up to a distance of $5D_d$ in the vertical direction and $10D_d$ in
298 the horizontal one (Figure 5). Initially, 2 VoF equations are solved with an implicit VOF solver, while an additional
299 VoF equation is solved after vapor is formed. For the spatial discretization of VoF equation, the Compressive scheme
300 is used [55], while momentum equation is spatially discretized with a second order scheme, where quantities at
301 cell faces are computed using a multidimensional linear reconstruction approach [56]. The energy equation is
302 spatially discretised with a first order upwind scheme. The local grid refinement technique [53] enhances the
303 accuracy of the computations at the interface region, while achieving low computational cost compared to a
304 simulation with a uniform grid of the same density. Base grid resolution is such that, with 6 levels of refinement,
305 the initial vapor bubble resolution is ~ 2 cpR, while the resolution corresponding to the outer droplet is 200 cpR.



307 Figure 5. Computational axisymmetric domain, with zoom at levels of local refinement around the HFO-air and HFO-water
308 interfaces.

309
310 In all examined cases, the W/HFO emulsion droplet contains two water sub-droplets which are located in the front
311 and the back of the oil droplet, in order to capture the interface rupturing; this may occur in both sides depending
312 on the local temperature. The emulsion droplet is placed at ambient pressure $p = 30$ bar and temperature $T_g =$
313 1000 K. The droplet's injection temperature is 360 K while the boiling temperatures of HFO and water are 660 K
314 and 506 K, respectively. The physical properties of HFO are representative of those used in marine engines. Liquid
315 density, dynamic viscosity and surface tension can be found in the work of [57], while thermal conductivity and
316 heat capacity are computed by empirical relationships provided by [58]; these were assumed constant without any
317 temperature dependence. The initial HFO droplet diameter is $D_{HFO} = 50$ μm , which is typical droplet size in sprays
318 [59], while the diameter of the embedded water droplets was selected equal to $D_w = 10$ μm . That size has been
319 also investigated in past studies [15, 60, 61]. At this point, it should be mentioned that it's rather complicated to
320 relate the sub-droplet size with the corresponding water content of the emulsion, since emulsions may contain
321 different amount of water sub-droplets but the same water content; in both cases it is expected a different
322 puffing/micro-explosion outcome. The superheat degree, which is an input parameter to the model, has been
323 selected equal to $\Delta T_s = 10$. The latter value corresponds to a St equal to 0.02 . For the aforementioned St and the
324 computed water-water vapor density ratio ($\rho_w/\rho_v = 60$), the OCASIMAT algorithm predicts with high accuracy the
325 bubble growth rate; according to Figure 4, the error is less than 0.2 . The examined Weber numbers in the cases
326 range from 40 to 190 , which correspond to droplet velocities in the range of 10 - 100 m/s. The latter is a typical
327 velocity range in HFO fueled engines [59]. The Ohnesorge number is calculated equal to 0.9 , implying that viscous
328 phenomena are important. The thermophysical properties and nondimensional numbers are summarized in the
329 following tables.

333
334
335
336
337
338
339
340
341
342
343
344
345
346
347
348
349
350
351
352
353

	Units	Water		HFO	Air
		Liquid	Vapor		
T	K	360	506	360	1000
ρ	kg m ⁻³	968	15	907	10.3
c_p	J kg ⁻¹ K ⁻¹	4195	3612	2020	1143
κ	W m ⁻¹ K ⁻¹	0.675	0.047	0.127	0.068
μ	kg m ⁻¹ s ⁻¹	3.2 10 ⁻⁴	1.69 10 ⁻⁵	0.032	4.3 10 ⁻⁵
h_{lv}	J kg ⁻¹	1.794 10 ⁶			

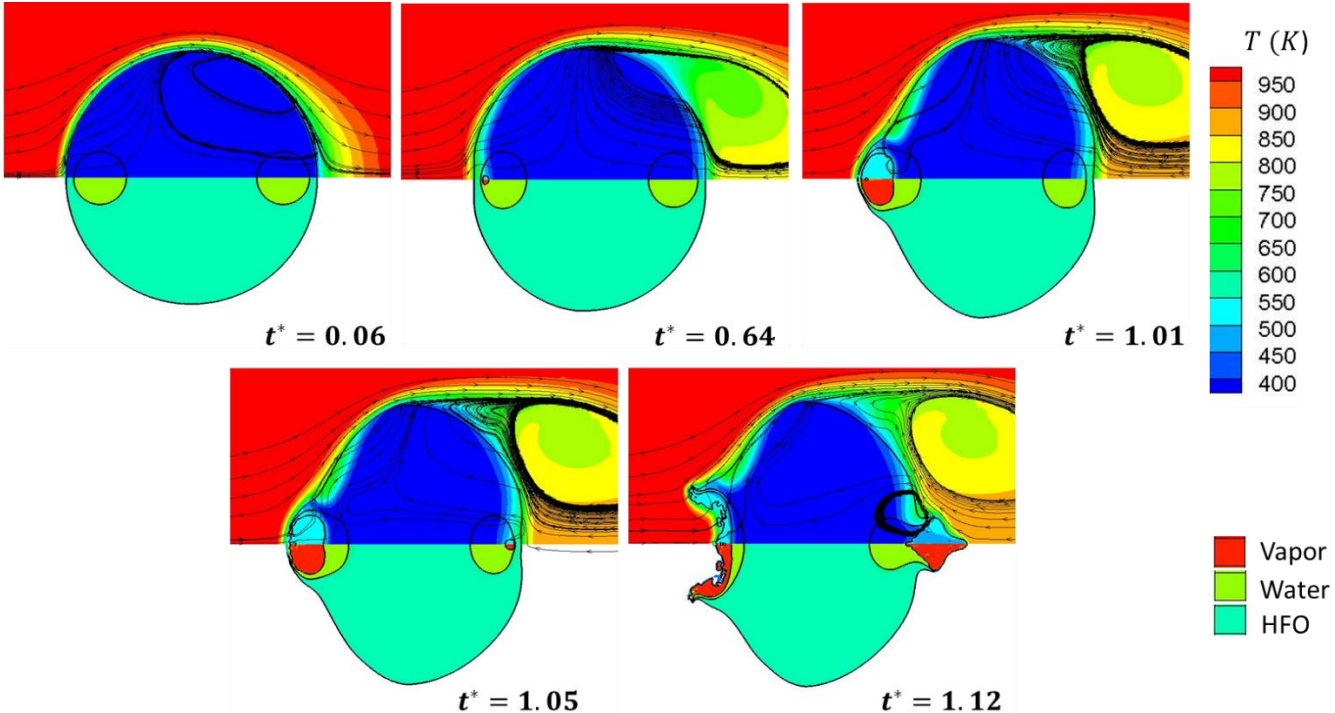
Table 1. Thermophysical properties (computed by [58]). The pressure was assumed constant at 30bar.

We_g	$\rho_g u_{rel}^2 D_{HFO} / \sigma$	70
Pe_{HFO}	$D_{HFO} u_{oil} / \alpha_{oil}$	200
Re_g	$\rho_g D_{HFO} u_{rel} / \mu_g$	720
Oh_{HFO}	$\mu_{HFO} / \sqrt{\rho_{HFO} \sigma D_{HFO}}$	0.9
St_w	$c_{pLW} \Delta T_s / h_{lv}$	2.3 10 ⁻²

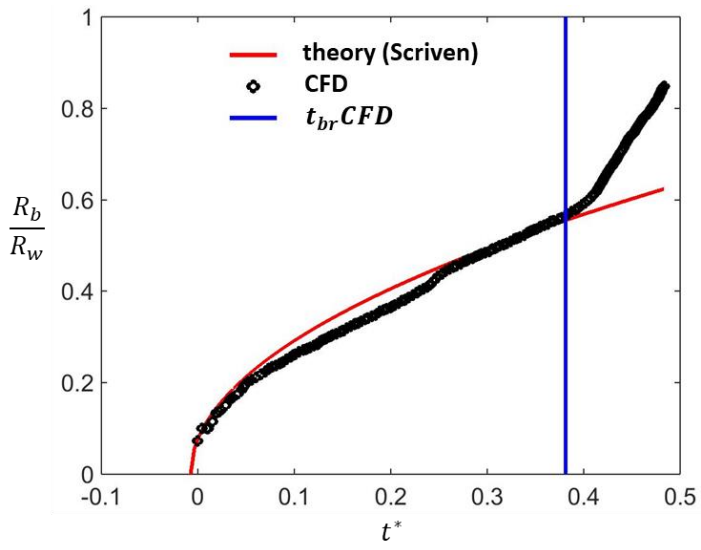
3.2.2 W/HFO emulsion droplet breakup

Here, W/HFO emulsion droplet breakup is examined for a reference case where the initial velocity of the air stream is $u_g = 60$ m/s, corresponding to *Weber number* $We=70$. The temporal evolution of the emulsion droplet is illustrated in Figure 6. The upper part shows the temperature field alongside with the streamlines, while in the lower part the contributing phases are illustrated. The time (t^*) is non-dimensionalised with the shear timescale t_{sh} . One can see that at the initial stage, steep temperature gradients are formed near the droplet interface. At $t^* = 0.06$, a temperature distribution is formed in the surrounding gas phase; the emulsion droplet is subjected to convective heating and the inner temperature profile tends to follow the streamlines; the inner droplet temperature has not increased much though. At the next time instance ($t^* = 0.64$), the same features in the gas phase are observed but the temperature of the front water sub-droplet has locally reached the superheat degree for the onset of bubble formation. As the criteria for the vapor generation have been fulfilled, the appearance of a vapor bubble is observed. The vapor bubble starts growing due to the temperature difference at its interface. The growth rate of the bubble formed in the upstream droplet is shown in Figure 7 in terms of the dimensionless equivalent bubble radius (this was obtained from the bubble volume). In the horizontal axis, the time instance of bubble formation has shifted to zero. As seen, the bubble radius grows in time according to \sqrt{t} , while the growth constant b found to be higher compared to the theoretical prediction. That deviation from theory is expected, since a number of assumptions is violated, i.e. bubble grows inside a droplet instead of an infinite pool, spherical asymmetry, shape deformation and bubble motion. Fragmentation of the HFO-air boundary occurs at $t^* = 1.01$ and water vapor is escaping in the ambient air; in the present work, this time instant is considered as the breakup initiation time. This feature is observed clearly at $t^* = 1.12$ (vapor phase indicated by red colour). The corresponding vapor bubble growth and breakup process occurs also, with a temporal delay, in the downstream region of the parent droplet. These results indicate that the breakup regime in this case is puffing, since partial breakup of the W/HFO droplet occurs. Finally, it has to be noted that the droplet deformation due to aerodynamic

379 forces plays a minor role here, since the combination of We and Oh examined corresponds to a relative slow
 380 deformation process.



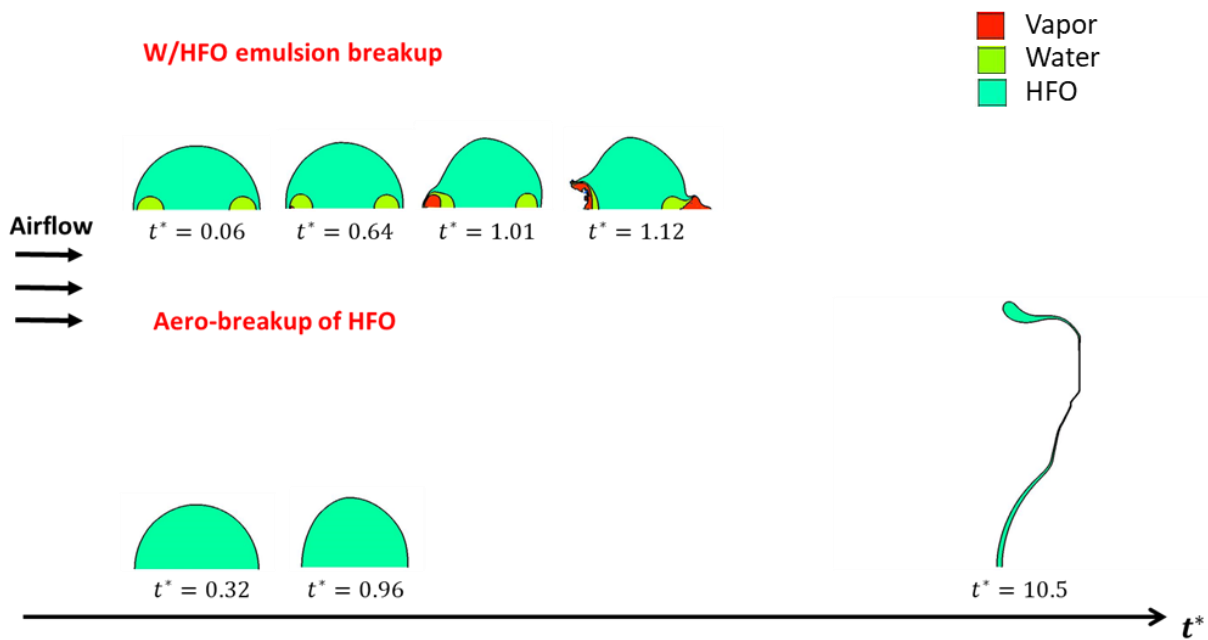
381
 382 Figure 6. Temporal evolution of emulsion droplet breakup. Upper part: Temperature profile. Lower part: HFO, Water liquid
 383 and Water vapor phases indicated by cyan, green and red respectively.



384
 385 Figure 7. Nondimensional vapor bubble radius predicted by Scriven solution (red solid line) and CFD simulation (black scatter
 386 symbols) for the front bubble with $We = 70$ and a corresponding breakup initiation time (vertical blue line)

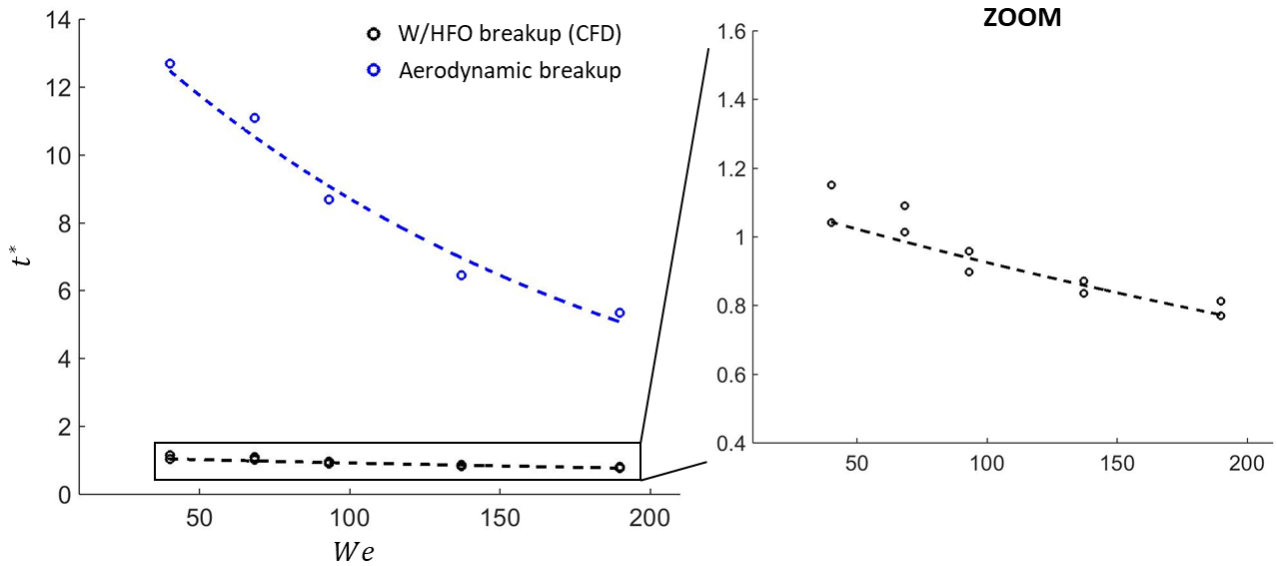
388 3.2.3 Parametric study with Weber number

389 Having identified the physical phenomena occurring during the coupled thermal and aerodynamic loading of the
 390 droplet, the effect of We on the breakup initiation time of the W/HFO emulsion droplet is examined in detail. For
 391 the examined range of We , simulations are also performed for neat HFO droplets in order to predict their breakup
 392 initiation time due to aerodynamic forces and compare it against those when puffing/micro-explosion is accounted
 393 for. For the default Weber number case ($We = 70$), the temporal evolution of the neat HFO droplet (lower panel)
 394 is illustrated in Figure 8, alongside with those of the benchmark W/HFO emulsion cases (upper panel). The neat
 395 HFO droplet breaks under aerodynamic forces at $t^* = 10.5$, which is an order of magnitude longer compared to
 396 the breakup initiation time of W/HFO emulsion. This clearly reveals the droplet fragmentation acceleration when
 397 using emulsified droplets in viscous fuels.



399 Figure 8. Temporal evolution of W/HFO emulsion droplet (Upper panel) and neat HFO droplet (Lower panel) for We number
400 equal to 70.
401

402 In the left panel of Figure 9, the dependence of the breakup initiation time on the We is illustrated. For the case of
 403 aerodynamic droplet breakup (blue scatter symbols), the breakup initiation time decreases strongly with increasing
 404 We , which is in accordance with several past studies [54, 62-69]. Regarding the breakup of emulsified droplets
 405 (black scatter symbols), the right-hand side panel of Figure 9 shows a weakly decreasing dependence on We . In
 406 each We correspond two black scatters, which stand for breakup initiation time of the upstream and downstream
 407 side of the droplet emulsion. It is observed that the difference between the two time instances decreases as We
 408 increases. Overall, it is important to mention that the emulsion breakup occurs 4-10 times faster than the
 409 aerodynamic breakup. The latter trend indicates that puffing/micro-explosion process can speed up the breakup of
 410 the droplet relative to the mechanism of the aerodynamic breakup for the range of conditions ($Oh \approx 1, We <$
 411 200) examined here.

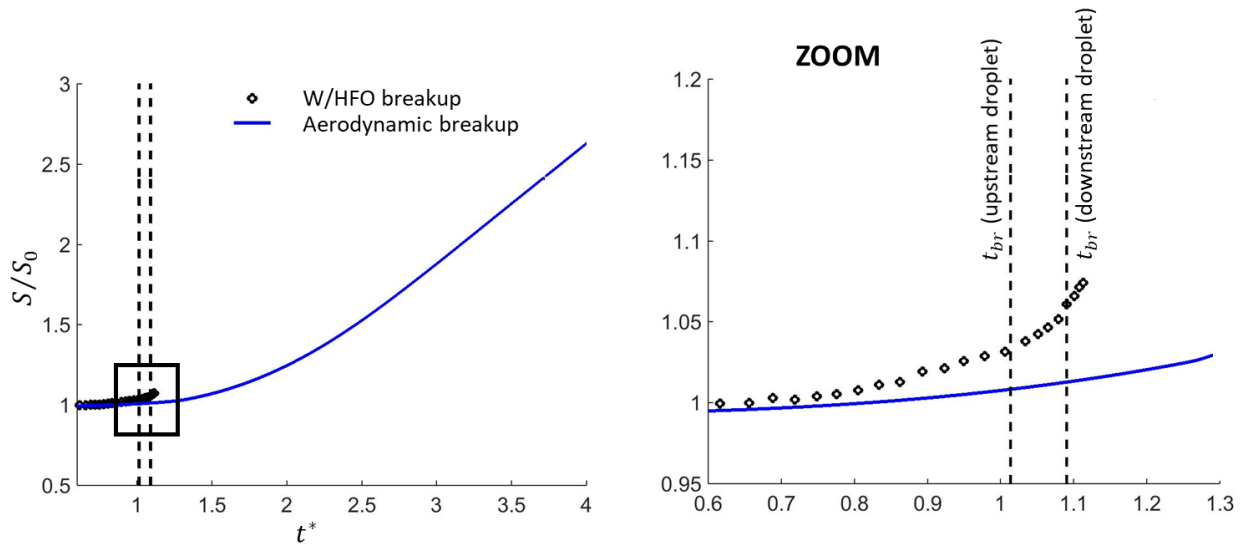


412
 413 Figure 9. Breakup time of W/HFO emulsion droplet for a range of We (black scatter symbols). Aerodynamic breakup of neat
 414 HFO droplet for the corresponding range of We (blue solid line).
 415

416 3.2.4 Droplet deformation

417 In the previously presented Figure 6, it was observed that the W/HFO emulsion droplet was slightly deformed after
 418 its breakup initiation time compared to its initial spherical shape. It is expected that if a larger amount of water sub-

419 droplets is present in the parent droplet, simultaneous (and/or successive) boiling will occur in each sub-droplet
 420 and the induced deformation will be accelerated. This process is indicated in Figure 10, where the dimensionless
 421 surface area of the W/HFO emulsion droplet and the neat HFO droplet are illustrated; the surface area of the latter
 422 has significantly increased up to the breakup initiation time. It is clear that the surface area of the W/HFO emulsion
 423 increases during the successive explosion events caused by the downstream and upstream water sub-droplet.



424

425 Figure 10. Temporal evolution of the dimensionless surface area of the W/HFO emulsion (scatter symbols) and the neat HFO
 426 droplet (blue line)

427

428 4. Conclusions

429 The heating and interface dynamics leading to fragmentation of immiscible heavy fuel oil-water droplets, termed
 430 as W/HFO emulsions, was examined numerically by solving the incompressible Navier-Stokes and energy
 431 conservation equations alongside with three sets of VoF transport equations utilised for resolving the interfaces
 432 between the co-existing HFO, water liquid and water vapour. A key feature of the puffing/micro-explosion
 433 phenomenon is the explosive boiling of embedded water droplets. To resolved this, an algorithm predicting the
 434 nucleation water vapour at a certain superheat degree, typical for water-HFO interfaces, was utilised. This algorithm
 435 scans the temperature field of liquid water and forms a vapor bubble with pre-defined properties. The subsequent
 436 vaporization rate of the growing bubbles inside the water sub-droplet, was computed with the OCASIMAT

437 algorithm. The latter was validated for the idealised configuration of a vapor bubble growing inside an infinite
438 superheated liquid pool, against a theoretical solution. Next, numerical simulations of W/HFO emulsion droplet
439 breakup were performed. A benchmark case was presented for a W/HFO emulsion droplet with an initial velocity
440 $u_g = 60$ m/s, at ambient pressure $p = 30$ bar and temperature $T_g = 1000$ K. Two water sub-droplets were
441 initialised inside the parent HFO liquid droplet, downstream and upstream relative to the surrounding air flow
442 motion. It was observed that the atomization of the emulsion droplet is puffing-induced. Next, the model was used
443 to perform numerical simulations of W/HFO emulsion droplet breakup for a range of We that are representative
444 for Diesel engines. The diameter of HFO droplet and Oh ($50 \mu\text{m}$ and 0.9 , respectively) were kept unchanged for all
445 parametric cases investigated. Predictions from those simulations have been compared with those corresponding
446 to cases of aerodynamic breakup of neat HFO droplets having identical properties and initial conditions as those of
447 the corresponding emulsions. It was revealed that for the viscous fuel examined ($Oh > 1$) puffing/micro-explosion
448 speeds up the droplet breakup by almost an order of magnitude relative to the aerodynamic breakup. This was
449 more evident for relatively low We , while increasing the We resulted in faster droplet breakup.

450

451 **Acknowledgement**

452 Financial support from the MSCA-ITN-ETN of the European Union's H2020 programme, under REA grant agreement
453 n. 675676 is acknowledged.

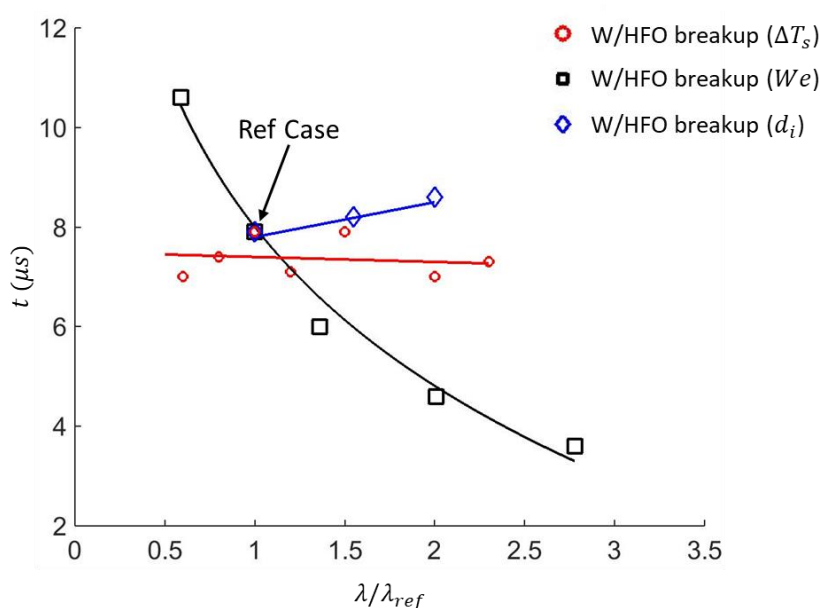
454

455 **Appendix A. Effect of bubble surface depth and superheat degree on W/HFO emulsion breakup**

456 In subsection 2.2 a mechanistic model that is responsible for bubble formation inside the embedded water sub-
457 droplet was presented. The criteria under which a vapor bubble is generated in a computational cell, are that the
458 latter should reach a superheat degree (ΔT_s) and have a specific distance (d_i) from the water-HFO interface. Both
459 are input parameters of the model. A parametric study with d_i and ΔT_s is performed, for the reference case of
460 $We = 70$, in order to investigate their sensitivity on emulsion breakup time. The results are compared against the
461 parametric study of breakup time with We (Figure 9). Horizontal axis of Figure 11 indicates the aforementioned

462 parameters $\lambda = \langle d_i, \Delta T_s, We \rangle$, which are normalised with the examined values of the reference case. Results
 463 show that breakup initiation time slightly increases with d_i (blue scatter symbols); this is expected since it takes
 464 some time for heat transfer to occur deeper inside the water sub-droplet and result to subsequently formation of
 465 the water vapour bubble. Regarding the effect of superheat degree, it seems that breakup initiation time slightly
 466 changes (red scatter symbols) without having a clear trend with ΔT_s . Finally, it is observed that both parameters
 467 are much less sensitive to breakup initiation time compared to the effect of We (black scatter symbols); when the
 468 latter increases five times, the breakup initiation time becomes approximately an order of magnitude lower.

469



470

471 Figure 11. Breakup initiation time of W/HFO emulsion with superheat degree (red scatter symbols), bubble surface depth
 472 (blue scatter symbols) and We (black scatter symbols)

473

474 **References**

475 1. Reitz, R., et al., *IJER editorial: the future of the internal combustion engine*. 2020, SAGE Publications Sage
 476 UK: London, England.

477 2. The Outlook for Energy: A View to 2040. Exxon Mobil Corporation, 2019.

478 3. Kolev, N.I., *Forced convection boiling*, in *Multiphase Flow Dynamics 3: Thermal Interactions*, N.I. Kolev,
 479 Editor. 2012, Springer Berlin Heidelberg. p. 213-243.

- 480 4. Kumar, M.S., J. Bellettre, and M. Tazerout, *The use of biofuel emulsions as fuel for diesel engines: a review*.
481 2009, SAGE Publications Sage UK: London, England.
- 482 5. Qin, D., et al., *IPCC, 2007: Summary for Policymakers*. 2007.
- 483 6. Jegannathan, K.R., et al., *Production of biodiesel using immobilized lipase—a critical review*. *Critical Reviews*
484 *in Biotechnology*, 2008. **28**(4): p. 253-264.
- 485 7. Tan, T., et al., *Biodiesel production with immobilized lipase: a review*. *Biotechnology advances*, 2010. **28**(5):
486 p. 628-634.
- 487 8. Tarlet, D., et al., *Formulation and combustion of emulsified fuel: The changes in emission of carbonaceous*
488 *residue*. *International journal of energy research*, 2010. **34**(8): p. 688-694.
- 489 9. Bedford, F., et al., *Effects of direct water injection on DI diesel engine combustion*. 2000, SAE Technical
490 Paper.
- 491 10. Tauzia, X., A. Maiboom, and S.R. Shah, *Experimental study of inlet manifold water injection on combustion*
492 *and emissions of an automotive direct injection diesel engine*. *Energy*, 2010. **35**(9): p. 3628-3639.
- 493 11. Basha, J.S. and R. Anand, *An experimental study in a CI engine using nanoadditive blended water–diesel*
494 *emulsion fuel*. *International journal of green energy*, 2011. **8**(3): p. 332-348.
- 495 12. Kadota, T. and H. Yamasaki, *Recent advances in the combustion of water fuel emulsion*. *Progress in energy*
496 *and combustion science*, 2002. **28**(5): p. 385-404.
- 497 13. Kumar, M.S., J. Bellettre, and M. Tazerout, *Investigations on a CI engine using animal fat and its emulsions*
498 *with water and methanol as fuel*. 2005, SAE Technical Paper.
- 499 14. Avedisian, C. and R. Andres, *Bubble nucleation in superheated liquid—liquid emulsions*. *Journal of colloid*
500 *and interface science*, 1978. **64**(3): p. 438-453.
- 501 15. Shinjo, J., et al., *Physics of puffing and microexplosion of emulsion fuel droplets*. *Physics of Fluids (1994-*
502 *present)*, 2014. **26**(10): p. 103302.
- 503 16. Shinjo, J., et al., *Modeling temperature distribution inside an emulsion fuel droplet under convective heating:*
504 *a key to predicting microexplosion and puffing*. *Atomization and Sprays*, 2016. **26**(6).
- 505 17. Shepherd, J.E. and B. Sturtevant, *Rapid evaporation at the superheat limit*. *Journal of Fluid Mechanics*, 2006.
506 **121**: p. 379-402.
- 507 18. Frost, D., *Dynamics of explosive boiling of a droplet*. *The Physics of fluids*, 1988. **31**(9): p. 2554-2561.
- 508 19. Ochoterena, R., et al., *Optical studies of spray development and combustion of water-in-diesel emulsion and*
509 *microemulsion fuels*. *Fuel*, 2010. **89**(1): p. 122-132.
- 510 20. Park, S., et al., *The characteristic of spray using diesel water emulsified fuel in a diesel engine*. *Applied*
511 *energy*, 2016. **176**: p. 209-220.
- 512 21. Zhu, M., et al., *An experimental investigation into the ignition and combustion characteristics of single*
513 *droplets of biochar water slurry fuels in air*. *Applied energy*, 2017. **185**: p. 2160-2167.
- 514 22. Califano, V., R. Calabria, and P. Massoli, *Experimental evaluation of the effect of emulsion stability on micro-*
515 *explosion phenomena for water-in-oil emulsions*. *Fuel*, 2014. **117**: p. 87-94.
- 516 23. Mura, E., et al., *Study of the micro-explosion temperature of water in oil emulsion droplets during the*
517 *Leidenfrost effect*. *Experimental Thermal and Fluid Science*, 2012. **43**: p. 63-70.
- 518 24. Fuchihata, M., T. Ida, and Y. Mizutani, *Observation of microexplosions in spray flames of light oil water*
519 *emulsions. II. Influence of temporal and spatial resolution in high speed videography*. *Nippon Kikai Gakkai*

- 520 Ronbunshu B Hen(Transactions of the Japan Society of Mechanical Engineers Part B)(Japan), 2003. **15**(6):
521 p. 1503-1508.
- 522 25. Watanabe, H. and K. Okazaki, *Visualization of secondary atomization in emulsified-fuel spray flow by*
523 *shadow imaging*. Proceedings of the Combustion Institute, 2013. **34**(1): p. 1651-1658.
- 524 26. Brennen, C.E., *Cavitation and bubble dynamics*. 2014: Cambridge University Press.
- 525 27. Rayleigh, L., *VIII. On the pressure developed in a liquid during the collapse of a spherical cavity*. The London,
526 Edinburgh, and Dublin Philosophical Magazine and Journal of Science, 1917. **34**(200): p. 94-98.
- 527 28. Forster, H. and N. Zuber, *Dynamics of vapor bubbles and boiling heat transfer*. AIChE Journal, 1955. **1**(4): p.
528 531-535.
- 529 29. Plesset, M. and S.A. Zwick, *The growth of vapor bubbles in superheated liquids*. Journal of Applied Physics,
530 1954. **25**(4): p. 493-500.
- 531 30. Scriven, L., *On the dynamics of phase growth*. Chemical engineering science, 1959. **10**(1-2): p. 1-13.
- 532 31. Van Stralen, S., *The growth rate of vapour bubbles in superheated pure liquids and binary mixtures: Part I:*
533 *Theory*. International Journal of Heat and Mass Transfer, 1968. **11**(10): p. 1467-1489.
- 534 32. Mikic, B., W. Rohsenow, and P. Griffith, *On bubble growth rates*. International Journal of Heat and Mass
535 Transfer, 1970. **13**(4): p. 657-666.
- 536 33. Shusser, M. and D. Weihs, *Explosive boiling of a liquid droplet*. International journal of multiphase flow,
537 1999. **25**(8): p. 1561-1573.
- 538 34. Zeng, Y. and F.L. Chia-fon, *Modeling droplet breakup processes under micro-explosion conditions*.
539 Proceedings of the Combustion Institute, 2007. **31**(2): p. 2185-2193.
- 540 35. Girin, O.G., *Dynamics of the emulsified fuel drop microexplosion*. Atomization and Sprays, 2017. **27**(5).
- 541 36. Sazhin, S., et al., *A simple model for puffing/micro-explosions in water-fuel emulsion droplets*. International
542 Journal of Heat and Mass Transfer, 2019. **131**: p. 815-821.
- 543 37. Guildenbecher, D., C. López-Rivera, and P. Sojka, *Secondary atomization*. Experiments in Fluids, 2009. **46**(3):
544 p. 371.
- 545 38. Nicholls, J. and A. Ranger, *Aerodynamic shattering of liquid drops*. Aiaa Journal, 1969. **7**(2): p. 285-290.
- 546 39. Nissar, Z., et al., *A model for puffing/microexplosions in water/fuel emulsion droplets*. International Journal
547 of Heat and Mass Transfer, 2020. **149**: p. 119208.
- 548 40. Zhang, Y., et al., *A new puffing model for a droplet of butanol-hexadecane blends*. Applied Thermal
549 Engineering, 2018. **133**: p. 633-644.
- 550 41. Avedisian, C. and I. Glassman, *Superheating and boiling of water in hydrocarbons at high pressures*.
551 International Journal of Heat and Mass Transfer, 1981. **24**(4): p. 695-706.
- 552 42. Avedisian, C.T., *The homogeneous nucleation limits of liquids*. Journal of physical and chemical reference
553 data, 1985. **14**(3): p. 695-729.
- 554 43. Perez-Raya, I. and S.G. Kandlikar, *Discretization and implementation of a sharp interface model for*
555 *interfacial heat and mass transfer during bubble growth*. International Journal of Heat and Mass Transfer,
556 2018. **116**: p. 30-49.
- 557 44. Hirt, C.W. and B.D. Nichols, *Volume of fluid (VOF) method for the dynamics of free boundaries*. Journal of
558 Computational Physics, 1981. **39**(1): p. 201-225.
- 559 45. Brackbill, J., D.B. Kothe, and C. Zemach, *A continuum method for modeling surface tension*. Journal of
560 computational physics, 1992. **100**(2): p. 335-354.

- 561 46. Kunkelmann, C. and P. Stephan, *CFD simulation of boiling flows using the volume-of-fluid method within*
562 *OpenFOAM*. Numerical Heat Transfer, Part A: Applications, 2009. **56**(8): p. 631-646.
- 563 47. Magnini, M., B. Pulvirenti, and J.R. Thome, *Numerical investigation of hydrodynamics and heat transfer of*
564 *elongated bubbles during flow boiling in a microchannel*. International Journal of Heat and Mass Transfer,
565 2013. **59**: p. 451-471.
- 566 48. Maki, K.L. and S. Kumar, *Fast evaporation of spreading droplets of colloidal suspensions*. Langmuir, 2011.
567 **27**(18): p. 11347-11363.
- 568 49. Sato, Y. and B. Ničeno, *A sharp-interface phase change model for a mass-conservative interface tracking*
569 *method*. Journal of Computational Physics, 2013. **249**: p. 127-161.
- 570 50. Sun, D., J. Xu, and Q. Chen, *Modeling of the evaporation and condensation phase-change problems with*
571 *FLUENT*. Numerical Heat Transfer, Part B: Fundamentals, 2014. **66**(4): p. 326-342.
- 572 51. Moussa, O., et al., *INSIGHT OF A WATER-IN-OIL EMULSION DROP UNDER LEIDENFROST HEATING USING*
573 *LASER-INDUCED FLUORESCENCE OPTICAL DIAGNOSTICS*. Atomization and Sprays, 2019. **29**(1).
- 574 52. Tanguy, S., et al., *Benchmarks and numerical methods for the simulation of boiling flows*. Journal of
575 Computational Physics, 2014. **264**: p. 1-22.
- 576 53. Malgarinos, I., N. Nikolopoulos, and M. Gavaises, *Coupling a local adaptive grid refinement technique with*
577 *an interface sharpening scheme for the simulation of two-phase flow and free-surface flows using VOF*
578 *methodology*. Journal of Computational Physics, 2015. **300**: p. 732-753.
- 579 54. Stefanitsis, D., et al., *Numerical investigation of the aerodynamic breakup of Diesel and heavy fuel oil*
580 *droplets*. International Journal of Heat and Fluid Flow, 2017. **68**: p. 203-215.
- 581 55. Ubbink, O. and R. Issa, *A method for capturing sharp fluid interfaces on arbitrary meshes*. Journal of
582 Computational Physics, 1999. **153**(1): p. 26-50.
- 583 56. Barth, T. and D. Jespersen. *The design and application of upwind schemes on unstructured meshes*. in *27th*
584 *Aerospace sciences meeting*. 1989.
- 585 57. Kyriakides, N., C. Chryssakis, and L. Kaiktsis, *Influence of heavy fuel properties on spray atomization for*
586 *marine diesel engine applications*. 2009, SAE Technical Paper.
- 587 58. Riazi, M., *Characterization and properties of petroleum fractions*. Vol. 50. 2005: ASTM international.
- 588 59. Wadhwa, A.R., V. Magi, and J. Abraham, *Transient deformation and drag of decelerating drops in*
589 *axisymmetric flows*. Physics of Fluids, 2007. **19**(11): p. 113301.
- 590 60. Khan, M.Y., et al., *A case study on the influence of selected parameters on microexplosion behavior of water*
591 *in biodiesel emulsion droplets*. Journal of Energy Resources Technology, 2017. **139**(2): p. 022203.
- 592 61. Kimoto, K., Y. Owashii, and Y. Omae, *The vaporizing behavior of the fuel droplet of water-in-oil emulsion on*
593 *the hot surface*. Bulletin of JSME, 1986. **29**(258): p. 4247-4255.
- 594 62. Pilch, M. and C. Erdman, *Use of breakup time data and velocity history data to predict the maximum size of*
595 *stable fragments for acceleration-induced breakup of a liquid drop*. International journal of multiphase flow,
596 1987. **13**(6): p. 741-757.
- 597 63. Stefanitsis, D., et al., *Numerical investigation of the aerodynamic breakup of droplets in tandem*.
598 International Journal of Multiphase Flow, 2019. **113**: p. 289-303.
- 599 64. Stefanitsis, D., et al., *Numerical investigation of the aerodynamic breakup of a parallel moving droplet*
600 *cluster*. International Journal of Multiphase Flow, 2019. **121**: p. 103123.

601 65. Strotos, G., et al., *Non-dimensionalisation parameters for predicting the cooling effectiveness of droplets*
602 *impinging on moderate temperature solid surfaces*. International Journal of Thermal Sciences, 2011. **50**(5):
603 p. 698-711.

604 66. Strotos, G., et al., *Numerical investigation of aerodynamic droplet breakup in a high temperature gas*
605 *environment*. Fuel, 2016. **181**: p. 450-462.

606 67. Strotos, G., et al., *Aerodynamic breakup of an n-decane droplet in a high temperature gas environment*.
607 Fuel, 2016. **185**: p. 370-380.

608 68. Strotos, G., et al., *Predicting droplet deformation and breakup for moderate Weber numbers*. International
609 Journal of Multiphase Flow, 2016. **85**: p. 96-109.

610 69. Strotos, G., et al., *Predicting the evaporation rate of stationary droplets with the VOF methodology for a*
611 *wide range of ambient temperature conditions*. International Journal of Thermal Sciences, 2016. **109**: p.
612 253-262.

613
614
615
616
617
618
619
620
621
622
623
624
625
626